Turkish Journal of Electrical Engineering & Computer Sciences

http://journals.tubitak.gov.tr/elektrik/

Research Article

Turk J Elec Eng & Comp Sci
(2015) 23: 853 – 872

doi:10.3906/elk-1303-139

Detection of microcalcification in digitized mammograms with multistable cellular neural networks using a new image enhancement method: automated lesion intensity enhancer (ALIE)

Levent CİVCİK[1,*], Burak YILMAZ[1], Yüksel ÖZBAY[1], Ganime Dilek EMLİK[2]
[1]Department of Electrical & Electronics Engineering, Selçuk University, Konya, Turkey
[2]Department of Radiology, Meram Medical Faculty, Necmettin Erbakan University, Konya, Turkey

Received: 19.03.2013 • **Accepted/Published Online:** 01.06.2013 • **Printed:** 30.04.2015

Abstract: Microcalcification detection is a very important issue in early diagnosis of breast cancer. Generally physicians use mammogram images for this task; however, sometimes analyzing these images become a hard task because of problems in images such as high brightness values, dense tissues, noise, and insufficient contrast level. In this paper, we present a novel technique for the task of microcalcification detection. This technique consists of three steps. The first step is focused on removing pectoral muscle and unnecessary parts from the mammogram images by using cellular neural networks (CNNs), which makes this a novel process. In the second step, we present a novel image enhancement technique focused on enhancing lesion intensities called the automated lesion intensity enhancer (ALIE). In the third step, we use a special CNN structure, named multistable CNNs. After applying the combination of these methods on the MIAS database, we achieve 82.0% accuracy, 90.9% sensitivity, and 52.2% specificity values.

Key words: Mammogram, microcalcification, cellular neural networks, image processing, image enhancement, automated lesion intensity enhancer, pectoral muscle

1. Introduction

Breast cancer is a common problem, occurring at a rate of more than 1 million people among women worldwide. Breast cancer incidence in Turkey is 42.7 per 100,000. Among Turkish women, in the top 10 cancers, the incidence of breast cancer ranks first, at 35.47% [1].

Depending on the effect of early diagnosis and improved treatment methods, death rates related to breast cancer have decreased in recent years [2]. Therefore, early diagnosis of breast cancer plays a very important role for women. Unfortunately, close to 30% of breast cancer cases are not detected [3,4].

There are some signs for breast cancer detection. Calcium deposits (microcalcifications) are one of the most important indicators. There is no exact definition for the shape of the microcalcifications. Microcalcifications usually appear as fragments of 0.1 to 2 mm wide in mammogram images. Microcalcifications in a mammogram appear as tiny bright spots and are one of the most difficult images for physicians to detect, especially in mammograms obtained from dense breast tissues. Microcalcification clusters are defined as 3 or more microcalcifications grouped in areas smaller than 1 cm^2 [5]. Detection of microcalcifications is a vital task in the early diagnosis of breast cancer. Image processing and artificial intelligence techniques serve as useful tools for helping physicians (especially less experienced ones) in mammogram reading.

*Correspondence: lcivcik@selcuk.edu.tr

There are a large number of approaches for segmentation of mammogram images, such as fuzzy logic methods, neural networks, and statistical methods. There are also shape-based classification techniques in the literature, such as Le Gal classification [6] or BI-RADS classification. In some studies, high-frequency components in the image spectrum are also used in determining data [7,8]. Many researchers combine these methods for better results. Generally features extracted from each pixel are presented to a trained classifier for detection and classification of the candidates. These kinds of methods are often followed by a postprocessing stage in order to reduce the false positive rate [7,9,10].

As one of the biomedical image types, mammograms are generally handled in 2D spaces. The great size of these images makes it harder to analyze them with pixel-based algorithms. Hence, cell-based algorithms give better and faster results, especially in tiny particle detection tasks like microcalcifications. In this study, cellular neural networks (CNNs) are used because of their cell-based nature.

CNNs were introduced in previous studies [11–13]. CNNs are described as interconnections of cells that are defined by a nonlinear state equation. These structures have been used in applications like image processing, pattern recognition, cryptography, and many other fields.

CNNs use matrices called templates for these tasks and every task needs a specific template. The training process of CNNs aims to obtain appropriate template matrices for the desired output. There are many varieties of CNN templates, like adaptive templates, linear templates, and cloning templates [14–21].

Although the cell-based algorithms have good yields, they can still encounter some obstacles during mammogram image analysis because of the nature of these images. Some tissues in breasts can cause adverse effects in mammogram images. For instance, fatty tissues increase the general intensity levels of the entire image. Hence, in this case, cell-based classification algorithms can miss microcalcifications because of the intensity level of the surrounding tissue. To increase the efficiency of the algorithms most of the time, the data should be preprocessed. In this step, a variety of image preprocessing and enhancement methods are applied depending on the nature of the image. There are many methods developed in this area.

In this paper, we propose a new approach, called the automated lesion intensity enhancer (ALIE), based on histogram adaptation methods. This method involves image analysis and a linear combination technique. The technique aims to decrease the effects of the tissues with high intensity levels and increase the detectability of the microcalcifications.

The method is followed by the multistable CNN algorithm for extracting possible microcalcification spots. A classification process is then applied to these extracted data for precision. We used the Mammographic Image Analysis Society (MIAS) database [22] because MIAS is a well-known, commonly used database in mammogram studies. In our study, we chose the digitized MIAS database because digitized mammograms are noisier than digital mammograms; hence, we evaluated our algorithms performance on noisy images.

There have not been many studies using CNNs in the process of detecting microcalcifications in mammograms in the literature. In this study, we used the ALIE algorithm for preprocessing the mammogram image and preparing the image for the CNN algorithm. From this point of view, our study demonstrates a new method.

2. Cellular neural networks

CNNs were introduced in 1988 [11–13]. CNNs are described as 2D cell arrays with local cell interconnections [11]. The structure of CNNs is based on cellular automata and a neural network architecture [23]. The main difference between conventional neural networks and CNNs is that the CNNs have a local connectivity property. Since this structure resembles the human retina, CNNs can be used as image processing tools in various manners, including medical image processing and segmentation tasks [23,24].

In digital medical image processing, CNNs can be thought of as cellular programmable multidimensional processing arrays with distributed logic and memory [25,26]. Training CNNs for a specific task is called template learning. CNN template learning is the determination of the values in the template of a CNN that affect the general dynamics of the structure. The learning process creates a stable connection network for the specified task. CNNs consist of cells placed as 2D arrays. Every cell in the structure is related to nearby neighboring cells, as presented in Figure 1 [12,13].

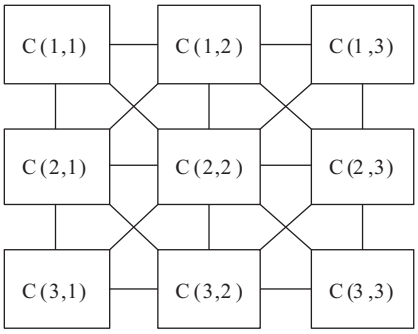

Figure 1. CNN cell structure.

A CNN cell is described as a normalized differential state equation (Eq. (1)). The basic CNN cell has a capacitor for giving it first-order dynamics, and neighboring cells are coupled with each other through nonlinear controlled sources. The dynamics of the CNN is described by:

$$\frac{d}{dt}x_{i,j}(t) = \sum_{k,l\in N} A_{k,l}y_{i+k,j+k}(t) + \sum_{k,l\in N} B_{k,l}u_{i+k,j+k} + I. \tag{1}$$

Nonlinearity of output is defined by Eq. (2).

$$y\,(x) = \frac{1}{2}\left[|x-1| - |x+1|\right] \tag{2}$$

The input, state, and output, represented by $u_{i,j}$, $x_{i,j}$, and $y_{i,j}$, respectively, are defined in $0 \leq I \leq N1$ and $0 \leq j \leq N2$.

A template contains the combination of a triplet{A, B, I} for the template learning, where A consists of all arguments a_{kl}, and B represents the values b_{kl}. In the structure of CNNs A and B, matrices are square matrices such as 3 × 3, 5 × 5, etc. The threshold is generally a one-dimensional scalar, but it can also be described as a matrix with the same size as the A and B matrices. In our study we used 3 × 3 templates.

The effects of the templates on equations can be described in block diagram form, as shown in Figure 2 [12,13]. The correlation sums in the equation can be written as convolutions by template reflection. From the diagram, it can be seen that the B template forms a simple feedforward finite impulse response filtered version of the input, which itself can be considered as static input to the rest of the system. On the other hand, the A template is operating in a feedback loop along with nonlinearity, a feature that gives interesting behavior [27].

In some cases, especially in image segmentation tasks, one other property of CNNs, multistability, plays a useful role. In the conventional CNN cell structure, the output function is defined as a piecewise linear function called unit saturation. This structure is common for all CNN-based tasks. The unit saturation function can be

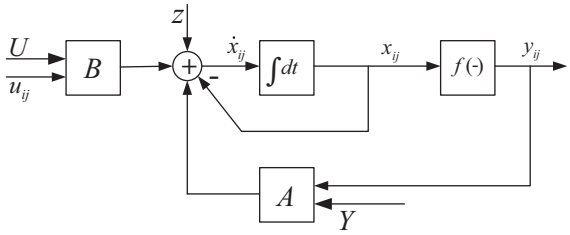

Figure 2. CNN's cell model.

defined as follows [27].

$$f(x) = \left\{ \begin{array}{cc} 1 & x \geq 1 \\ x & -1 < x < 1 \\ -1 & x \leq -1 \end{array} \right\} \tag{3}$$

The CNN's multistability property requires another definition for the output function. In a multistable CNN cell, every property is the same as in the normal CNN cell, but the output function differs from the standard unit saturation function. There are many possible output functions for multistable CNN cells, such as polynomial functions of different ranks or piecewise nonlinear functions with more slopes [28]. This piecewise function can be defined as follows.

$$f(x) = \left\{ \begin{array}{cc} 1 & x \geq 1 \\ m_1 x & 0 \leq |x| \leq b \\ m_2 x & b < |x| \leq c \\ -1 & x \leq -1 \end{array} \right\} \tag{4}$$

In this equation, there are slopes, and b and c are the breaking points of the equation. More slopes and breaking points can be added by defining new definition intervals. Because of the chaotic trend of CNNs, this definition must preserve the continuity of the output function. Undefined intervals or points are not allowed, as this can cause unstable or oscillatory behaviors [28].

3. Enhancement of mammographic images

Many researchers are working on computer-based image processing to help radiologists in the detection of breast cancer. One of the most important parts of these studies is the image enhancement stage. Image enhancements include noise reduction, background removal, histogram manipulation, sharpening, gray level, and contrast manipulation. One of the basic goals of mammogram image enhancement is to arrange the contrast between shape and background or to sharpen the edge of the image [29].

Various studies have been done on mammographic image enhancement. Photographic unsharp masking [30,31], digital unsharp masking [32], and spatial bandpass filtering [33] have been used to enhance mammograms. Chen et al. [31] studied an automatic method for optimized image contrast enhancement. Panetta et al. [32] performed edge-preserving contrast enhancement. Kosheleva et al. [34] used the selective median filtering method, which is a modification of the median filter operation.

3.1. Techniques of enhancement of mammographic images

In general, image enhancement, or the preprocessing step, deals with contrast adjustment, background removal, noise reduction, edge sharpening, and filtering.

Image enhancement includes many different methodologies and objectives. There are a large variety of algorithms developed on this area. These methods can be summarized by the following methods: histogram-based enhancement techniques as histogram equalization, contrast-based enhancement techniques as histogram adjustment, the region-based enhancement technique [30], and image enhancement using metaheuristic algorithms like genetic algorithms [35].

3.2. ALIE

In our study, a new histogram-based enhancement technique has been developed for improving and enhancing mammogram images for increasing the success rate in detection of microcalcifications.

The ALIE algorithm works on 8-bit integer-valued (scaled between 0 and 255) gray scale images, and the minimum resolution must be 1024 × 1024. Our method works on images with 0–255 gray value distributions. While working on other kinds of images, the image should be normalized to 0–255 gray values. The algorithm affects the entire image and preserves the gray values of lesions such as microcalcifications while darkening the other areas. It consists of 22 steps, shown in the flowchart in Figure 3. At the beginning, the algorithm calculates some index values and some coefficients from the histogram of the entire image, and then generates two more images using these values. The generated images preserve pixel location information, while one of them is generated by subtraction of the dark index value from the original image and the other one is generated by adding the light index value to the original image. After generating these images, the algorithm uses linear combination techniques and combines all three images for generating the enhanced final image. Generally median and average filtering is dangerous for mammograms, as filtering can cause loss of microcalcifications in the mammogram images, but in our algorithm the filtering steps are applied to support the final image, not to generate it. In the final step, we apply the last linear combination between the original image and the generated supporting image; hence, microcalcification locations on the original image still persist and no microcalcifications are lost. The ALIE method consists of 22 steps. The ALIE algorithm is given below as pseudocode and a flowchart.

ALIE (Source_Image // Read the image to be enhanced) {

Sharpened=unsharp(Source_image); //Apply unsharp mask on image

H=histogram(Sharpened); //Generate grayscale histogram for the image

H_W =H(5:255); // Subtraction of fully black region from histogram by thresholding

DH= H_W(1:125); // Dark region of the histogram

LH=H_W(126:255); // Light region of the histogram

DM=median(DH); // Median value of the dark region of the histogram

LM=median(LH); // Median value of the light region of the histogram

D_I= find (DM); // Finding the value of the dark index where the value overreaches the median value of the dark region

L_I= find (LM); // Finding the value of the light index where the value overreaches the median value of the light region

D_image= Source_image – D_I; // Generating decreased image from source image

L_image= Source_image + L_I; // Generating increased image from source image

TR_Image1= linearcombinate(D_image, Source_image); // First transient image generated by linear combination of decreased image and source image

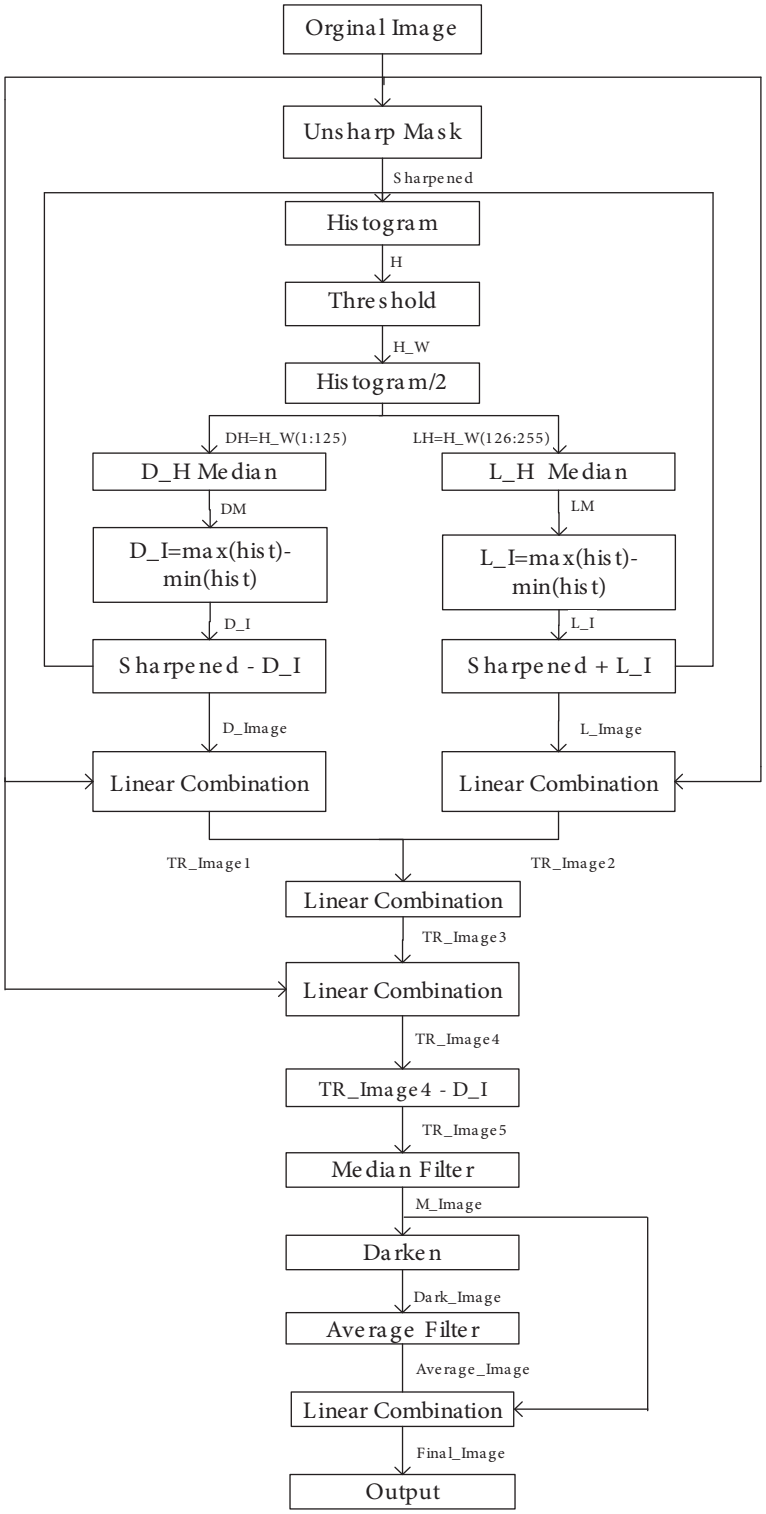

Figure 3. Flowchart of the ALIE algorithm.

TR_Image2= linearcombinate(L_image, Source_image); // Second transient image generated by linear combination of increased image and source image

TR_Image3= linearcombinate(TR_image1, - TR_image2); // Third transient image generated by linear combination of first transient image and negative second transient image

TR_image4= linearcombinate(TR_image3, Source_image); // Fourth transient image generated by linear combination of third transient image and source image

TR_image5= TR_image4 - D_I; // Fifth transient image generated by subtraction of dark index from fourth transient image

M_image= median_2d(TR_image5); // Median filtered image generated by applying a two-dimensional median filter on fifth transient image

Cbright= |L_I – D_I|; // Calculation of lightness coefficient

Cdark=Cbright-1; // Calculation of darkening coefficient

Dark_image=darken(M_image,Cdark); // Darkening median filtered image by using darkening coefficient

AvDark_image = average_filter(Dark_image); // Average filtered Dark_image

Final_image= linearcombinate (AvDark_image, M_image); Final image generated by linear combination of median filtered image and darkened image }

The flowchart of the algorithm (ALIE) is shown in Figure 3:

In Figure 4, the results of the ALIE algorithm applied to a mammogram image from the MIAS database (mdb222) are shown. Figure 4a is the source image file (mdb222), Figure 4b is a detail from the image, and Figure 4c is the detail from the final image with the same coordinates.

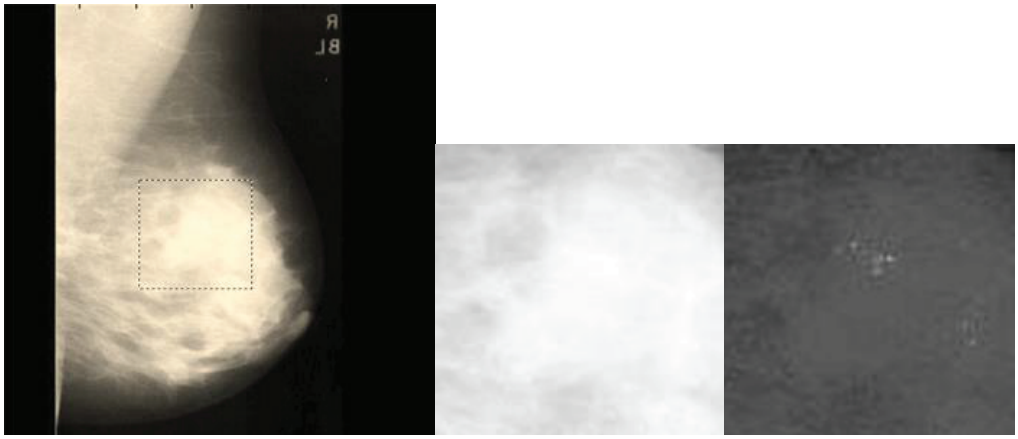

(a) (b) (c)

Figure 4. (a) Original mammogram image (mdb222) (1024 × 1024 resolution), (b) a cluster of microcalcifications in (a) (145 × 145 resolution), (c) the same image in (b) after ALIE algorithm (145 × 145 resolution).

Our proposed enhancement algorithm basically operates on a histogram of the source image and shifts the pixel values to the dark region of the histogram while protecting the pixel values of abnormalities, as shown in Figures 5a and 5b.

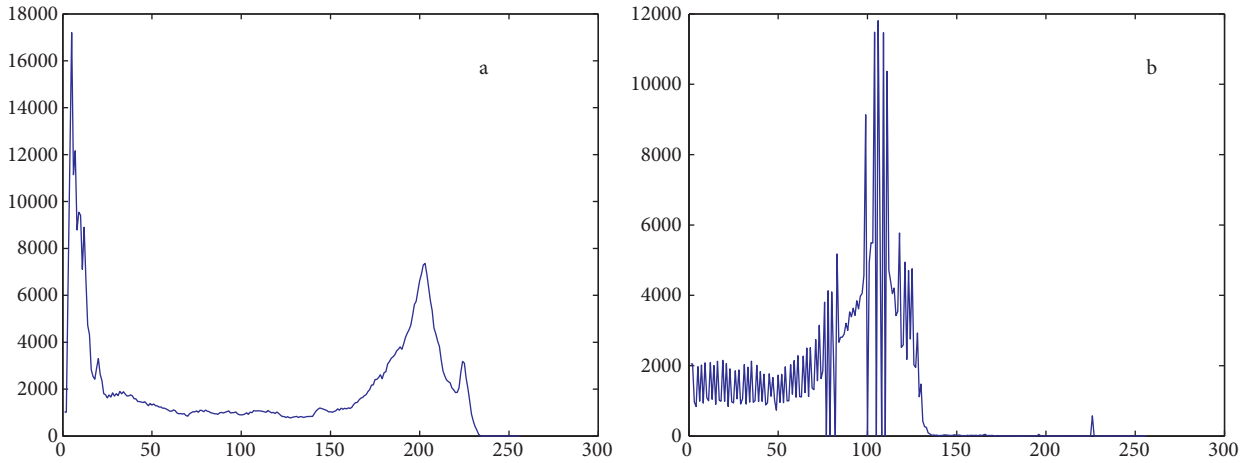

Figure 5. (a) Histogram of the source image, **(b)** histogram of the final image.

4. Detection of microcalcifications in digital mammograms with cellular neural networks

The method proposed in this study aims to detect suspicious particles in a mammogram image and inspect the microcalcifications among them. In this work, the mammogram image is first preprocessed for cleaning images from various noise signals. The pectoral muscle and extra partitions like labels are then removed. After this removal step, the background is set to absolute black value. The ALIE algorithm explained in Section 3 is used for enhancing probable lesions.

These preliminary steps are followed by a CNN algorithm for segmenting microcalcification particles from the image. Our proposed method is summarized by the flow chart in Figure 6.

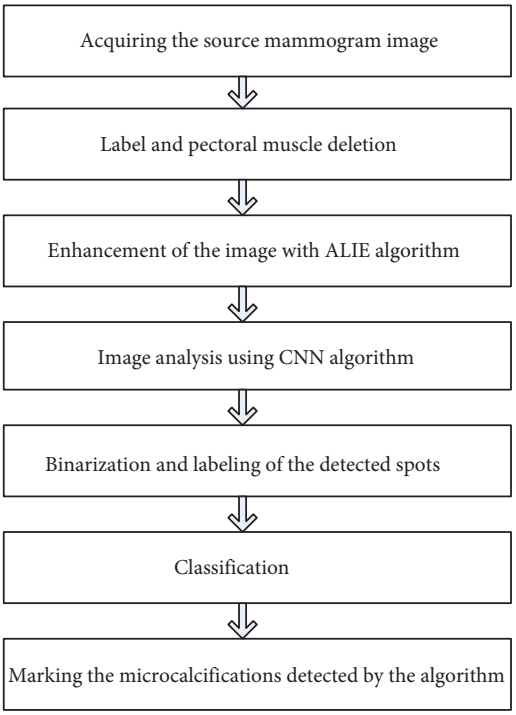

Figure 6. General flowchart of the proposed algorithm.

4.1. Extraction of pectoral muscle and labels

The pectoral muscle regions are generally very large areas in mammograms. They appear as a bright triangular region near the image corner [36]. Their high intensity value affects preprocessing steps adversely, especially the histogram equalization techniques. In our study, we needed to remove the pectoral muscle regions from the original image before starting to analyze it. After analyzing the image without the pectoral muscle and obtaining the coefficients, we used the images with pectoral muscles for enhancement with the ALIE algorithm. In some studies, especially in pixel-based and histogram-based techniques, removing these areas increases the robustness of the technique [37]. Some mammogram images can also include additional information, such as labels or direction information as high-intensity regions in the image's corner.

The microcalcifications neighboring the pectoral muscle could be lost in the pectoral muscle removal step. Hence, a cell-based method can be more accurate for this task. Therefore, we used the CNN algorithm for removing pectoral muscles to overcome this problem. In this paper, the CNN-based pectoral muscle and label removing algorithm has been used. The algorithm consists of two steps, both using CNN algorithms. In the first step, the CNN is trained with the recurrent perceptron learning algorithm (RPLA) [38] for detecting the entire breast in the image. The RPLA is used, generating A and B template matrices and an I bias value. The algorithm needs input and target datasets for calculating these values. In this study, an image obtained from the MIAS database is processed by a physician and a target dataset is generated. The target dataset includes the same images as the input dataset without unnecessary label parts, and also another dataset without the pectoral muscle regions.

The CNN templates obtained with RPLA for breast detection are shown below.

$$A = \begin{bmatrix} 0.8574 & 1.3370 & 0.9301 \\ 1.7550 & -1.6794 & 1.7550 \\ 0.9301 & 1.3370 & 0.8574 \end{bmatrix}, \begin{bmatrix} -1.7855 & -0.4677 & 1.6051 \\ -0.4438 & 0.4286 & -0.4438 \\ 1.6051 & -0.4677 & -1.7855 \end{bmatrix}, I = [0.8016]$$

After obtaining this CNN template, the entire MIAS dataset is presented to the CNN algorithm with this template. The output of this step was binary masking of the other regions to be set to zero value; hence, the label and unnecessary information are deleted.

In the second step, the CNN is also trained with a backpropagation algorithm for separating the pectoral muscle and breast tissue. In this step, the backpropagation algorithm was chosen because the results of this training were more precise. During the training task, the same dataset processed by the physician was used. The new template obtained is shown below.

$$A = \begin{bmatrix} 1.3372 & 1.8066 & 0.406 \\ 0.8926 & -8811 & 0.8926 \\ 0.0406 & 1.8066 & 1.3372 \end{bmatrix}, \begin{bmatrix} 1.4478 & -0.2689 & -1.4972 \\ -1.0045 & -0.2501 & -10045 \\ -1.4972 & -0.2689 & 1.4478 \end{bmatrix}, I = [-2.1454]$$

The output images of the second step were binary-valued images. Erosion and dilation operations were applied to these images to generate the binary mask. Finally, the pectoral muscle was placed on the upper left or right corner of the images. Removing this part from the original image gives the final mammogram image to be analyzed.

Removal of both the pectoral muscle and labels is position-based. The flowchart of the method is shown in Figure 7.

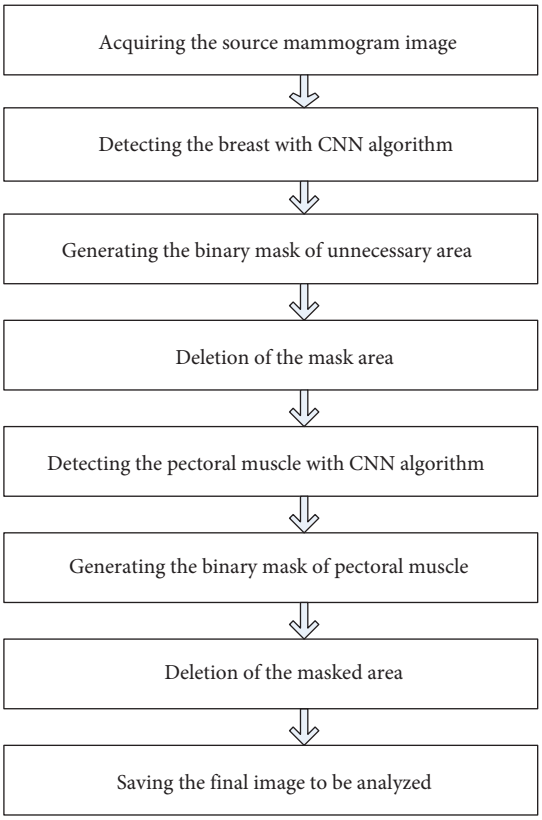

Figure 7. Flowchart of the pectoral muscle and label deletion algorithm.

Figure 8a is the original mammogram image, Figure 8b is the binary mask of the areas to be removed, Figure 8c shows the removed labels from the original image, Figure 8d is the binary mask of the pectoral muscle, and Figure 8e shows the removed pectoral muscles and labels from the original image.

The general CNN model as described previously in Figure 2 was used in this step, where the input parameter is $U = 0$ and the initial state parameter is $X_0 = Im_1$, where Im_1 describes the mammogram image to be cleared.

4.2. Lesion intensity enhancement using the ALIE algorithm

Mammograms are defined with low signal to noise ratios [39]. Noisy backgrounds and low contrast levels are the other problems. Hence, successful detection of microcalcifications needs a preprocessing step for enhancing the contrast levels and noise removal. In this study, the ALIE algorithm proposed in Section 3 is used for this task. The algorithm basically enhances the intensity level of abnormalities in mammogram images while reducing the intensity level of the background. The performance evaluation of the method is based on some global image enhancement evaluation criteria. These criteria are enhancement measure (EME), absolute mean brightness error (AMBE), and universal image quality index (UIQI) [40–43]. These evaluation methods work on the entire given image and especially evaluate the enhancement of intensity values and noise reduction between the original image and the enhanced image. The proposed algorithm runs on an entire image, too, and hence these global performance evaluation methods for evaluating the enhancement performance of the proposed algorithm were chosen. The performance evaluation results in this study are only for the image enhancement step; microcalcifications are handled in further steps.

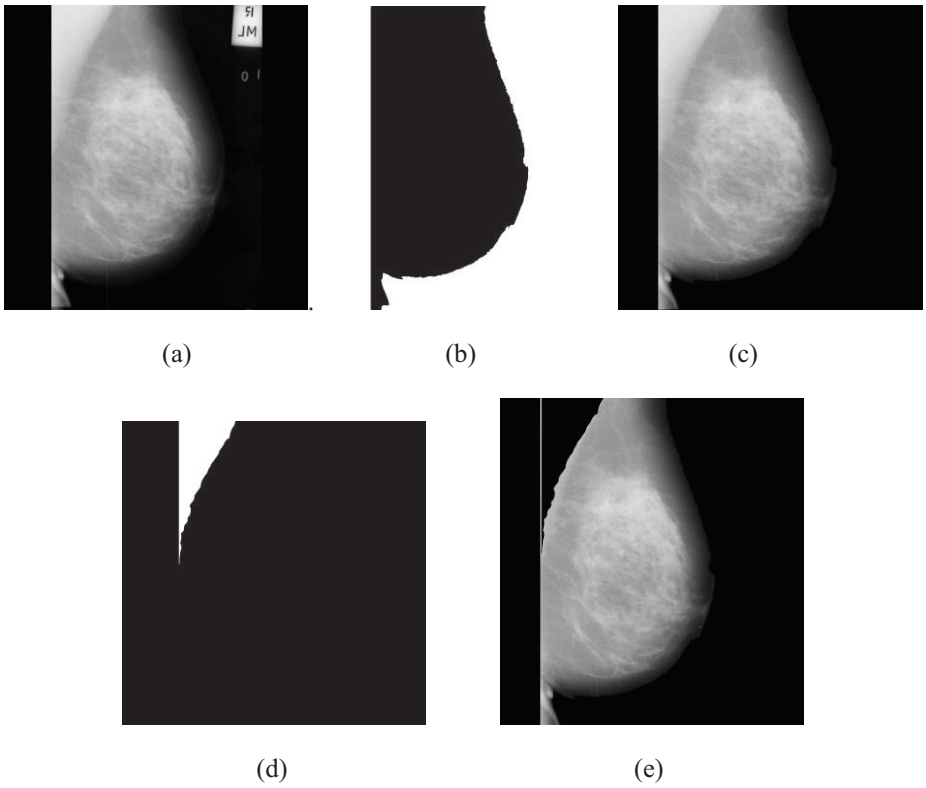

Figure 8. (a) Original mammogram image, **(b)** binary mask of the areas to be removed, **(c)** removed labels from the original image, **(d)** binary mask of pectoral muscle, **(e)** removed pectoral muscles and labels from the original image.

Formulation of the EME, AMBE and UIQI methods are as follows.

EME:

$$EME(f^{\wedge}) = EME_{\Phi}(f^{\wedge}) = \frac{1}{k^2}\sum_{m=1}^{k}\sum_{n=1}^{k} 20\log_2\frac{\max(f^{\wedge}[m,l])}{\min(f^{\wedge}[m,l])} \tag{5}$$

AMBE:

$$AMBE = |E(X) - E(Y)| \tag{6}$$

UIQI:

$$x = \{x_i \,|i = 1, 2, ..., N\} \text{ and } y = \{y_i \,|i = 1, 2, ..., N\} \tag{7a}$$

$$Q = \frac{4\sigma_{xy}\overline{x}\overline{y}}{(\sigma_x^2 + \sigma_y^2)\left[(\overline{x})^2 + (\overline{y})^2\right]} \tag{7b}$$

$$\overline{x} = \frac{1}{N}\sum_{i=1}^{N} x_i, \quad \overline{y} = \frac{1}{N}\sum_{i=1}^{N} y_i \tag{7c}$$

$$\sigma_x^2 = \frac{1}{N-1}\sum_{i=1}^{N}(x_i - \overline{x})^2, \quad \sigma_y^2 = \frac{1}{N-1}\sum_{i=1}^{N}(y_i - \overline{y})^2 \tag{7d}$$

$$\sigma_{xy}^2 = \frac{1}{N-1}\sum_{i=1}^{N}(x_i - \overline{x})(y_i - \overline{y}) \tag{7e}$$

The analysis results of these evaluation methods can be explained as follows.

High EME values mean overenhancement, which indicates local information loss. Very low values of EME mean that lesions or microcalcifications in dense tissues are not significantly enhanced [41].

High or low AMBE results mean that the enhancement process was insufficient [41]. It is preferred to keep this value at optimum levels for better contrast enhancement.

The UIQI value is placed between [0,1], where 1 means that the compared images are identical and 0 means that images are completely different. Values closer to 1 indicate that the enhancement is not sufficient, and values closer to 0 indicate that the image lost information while being enhanced.

Table 1 shows the quantitative performance measures compared to four different enhancing algorithms for all 22 numbers of the abnormal MIAS mammogram images in terms of microcalcification. The names and the formulations of the algorithms used to compare the enhancement performance of the ALIE are as follows.

Table 1. The quantitative performance measures compared with four different enhancing algorithms.

File name	EME				AMBE				UIQI			
	CLAHE	HE	US	ALIE	CLAHE	HE	US	ALIE	CLAHE	HE	US	ALIE
mdb209	6.8544	1.1254	3.0236	4.8819	4.3060	92.9838	0.2343	42.1025	0.3252	0.2612	0.7699	0.4304
mdb211	4.2508	0.4899	2.3722	3.8653	0.8624	102.7925	0.1862	38.0693	0.2964	0.2591	0.8257	0.5719
mdb212	3.8386	0.4701	2.2508	3.3067	0.3915	107.3968	0.1717	35.1812	0.2852	0.2299	0.8198	0.5565
mdb213	4.1072	0.3741	3.4118	2.8373	2.0027	127.8849	0.1257	28.3533	0.2568	0.1510	0.8490	0.6357
mdb214	3.6766	0.3346	2.3053	2.6689	3.6630	134.7640	0.1337	27.5365	0.2405	0.1398	0.8567	0.6400
mdb218	6.5972	1.5398	7.5311	2.9681	2.0345	78.5004	0.0946	37.9100	0.3876	0.2743	0.7522	0.4543
mdb219	5.0271	1.0538	3.0381	5.4180	0.9829	65.6234	0.2139	54.4590	0.3834	0.3762	0.8002	0.4837
mdb222	4.3953	0.5157	3.5442	2.6717	3.3751	104.6545	0.1290	31.2674	0.3035	0.2235	0.8243	0.5917
mdb223	3.9110	0.4188	4.0937	2.1033	3.9034	131.9944	0.1594	25.5154	0.2518	0.1672	0.8500	0.6628
mdb226	5.1382	0.6253	2.5388	2.5352	3.7635	122.1894	0.1786	29.2889	0.2523	0.1604	0.8113	0.5320
mdb227	3.1187	0.3236	1.9952	3.3876	0.1817	128.2633	0.1484	33.7320	0.2554	0.2104	0.8743	0.6748
mdb231	6.2917	1.6267	3.1722	8.2268	4.3110	69.3424	0.2504	59.9244	0.3783	0.3260	0.7667	0.4083
mdb236	6.4821	1.6844	7.7898	2.6527	1.0495	73.5060	0.1533	40.3257	0.3855	0.2883	0.7576	0.4696
mdb238	4.1378	0.7082	6.0282	3.6254	3.5619	105.7719	0.1463	37.7819	0.3322	0.2353	0.7996	0.5348
mdb239	6.3050	1.2701	3.5764	2.9201	1.2375	60.3121	0.2262	42.5752	0.3796	0.3081	0.7711	0.4792
mdb240	5.6353	1.1133	3.4734	3.5738	0.7391	59.8573	0.1412	37.4810	0.3643	0.2960	0.7726	0.4319
mdb241	3.6955	0.4614	3.4478	1.9479	1.4460	121.9848	0.1545	25.6532	0.2548	0.1836	0.8533	0.6773
mdb248	7.0739	1.4994	3.6003	4.1837	3.3134	82.2779	0.1865	42.6838	0.3407	0.2553	0.7547	0.4151
mdb249	4.9100	0.6826	2.7734	3.8794	0.1254	95.4229	0.1855	38.6819	0.3215	0.2649	0.8170	0.5471
mdb252	4.8098	0.7726	3.5740	4.2329	2.8939	105.3293	0.1585	39.7930	0.3074	0.2457	0.8117	0.5468
mdb253	5.8871	1.4970	6.7858	2.9696	1.3016	65.8996	0.1969	43.2067	0.4032	0.2777	0.7610	0.4772
mdb256	5.0626	1.2818	3.0258	3.9232	3.0347	74.2364	0.1732	48.3449	0.3452	0.2261	0.7590	0.4350
Average	5.0548	0.9031	3.7887	3.5808	2.2036	95.954	0.1703	38.1757	0.3204	0.2436	0.8026	0.5298

The unsharp mask (US):

$$\sigma_{xy}^2 = \frac{1}{N-1}\sum_{i=1}^{N}(x_i - \overline{x})(y_i - \overline{y}) \tag{8}$$

Contrast limited adaptive histogram equalization (CLAHE):

$$g = [g_{\max} - g_{\min}]\, p(f) + g_{\min} \tag{9}$$

$g_{\max}$ = maximum pixel value

$g_{\min}$ = minimum pixel value
g = computed pixel value
$p(f)$ = cumulative probability distribution function
Histogram equalization (HE):

$$p_n = \frac{\text{number of pixels with intensity}}{\text{total number of pixel}} \quad n = 0, 1, ..., L-1. \tag{10a}$$

The histogram equalized image g will be defined by:

$$g_{i,j} = floor((L-1)\sum_{n=0}^{f_{i,j}} p_n \tag{10b}$$

When Table 1 is examined, it can be seen that our proposed algorithm provides adequate enhancement values for these criteria. This enhancement success increases the success of the detection and classification steps.

$d(x,y)$ is the darkened version of $f_{sharp}(x,y)$ and $l(x,y)$ is the lightened version of f_{sharp} (x,y) after generating these versions of original image. The algorithm uses these images and generates a new set of images using linear combination techniques.

4.3. Image analysis using multistable CNN algorithm

After the image enhancement step, images become ready for the segmentation and classification step. Determination of the microcalcifications in mammograms with conventional CNN is difficult because of the intensity levels of the surrounding tissues. Intensity levels of these tissues are close to the intensity levels of microcalcifications. Hence, a method that can produce an output with multiple gray level values was required. In this paper, a multistable CNN algorithm is chosen. Multistable CNNs have a topology similar to that of conventional CNNs, but their output functions of the cells have more than two stationary states. This multioutput level property of the algorithm makes it useful for image decomposition tasks [28]. The A, B, and I values and parameters for the multistable CNN are also obtained with RPLA [38] for detecting the microcalcification spots. The target dataset for this training is also generated from the MIAS database using the information about the location of abnormalities given in the database.

The CNN template for extracting specific features in the enhanced mammogram image is obtained as below.

$$A = \begin{bmatrix} 0.3372 & 0.8066 & 0.2407 \\ -0.8926 & 5.3720 & -0.8926 \\ 0.2407 & 0.8066 & 0.3372 \end{bmatrix}, \begin{bmatrix} 1.4478 & -0.2689 & -1.4972 \\ -3.0045 & -0.2501 & -3.0045 \\ -1.4972 & -0.2689 & 1.4478 \end{bmatrix}, I = [-2.0655]$$

Because of the successful performance of the multistable CNNs on image segmentation, we also defined an output function with three regions. The selected function is defined in Eq. (11) and graphical representation of the function is given in Figure 9.

$$f(x) = \begin{Bmatrix} 1 & x \geq 1 \\ 0.55x & 0 \leq |x| \leq 0.7 \\ 0.25x & 0.7 < |x| \leq 1 \\ -1 & x \leq -1 \end{Bmatrix} \tag{11}$$

After applying the multistable CNN algorithm to enhanced images, the microcalcification spots are exposed. The classified spots are marked on the mammogram image for a physician's evaluation. In Figure 10, one of the processed and labeled mammogram images is shown. Figure 10a is the original image without pectoral muscles, Figure 10b is the image after the ALIE algorithm, Figure 10c is the image after the multistable CNN algorithm is applied, and Figure 10d is the classified and labeled microcalcification spot in the image.

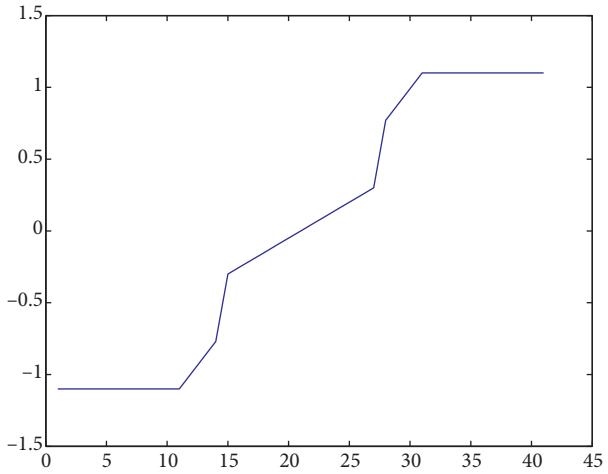

Figure 9. Output function of multistable CNN.

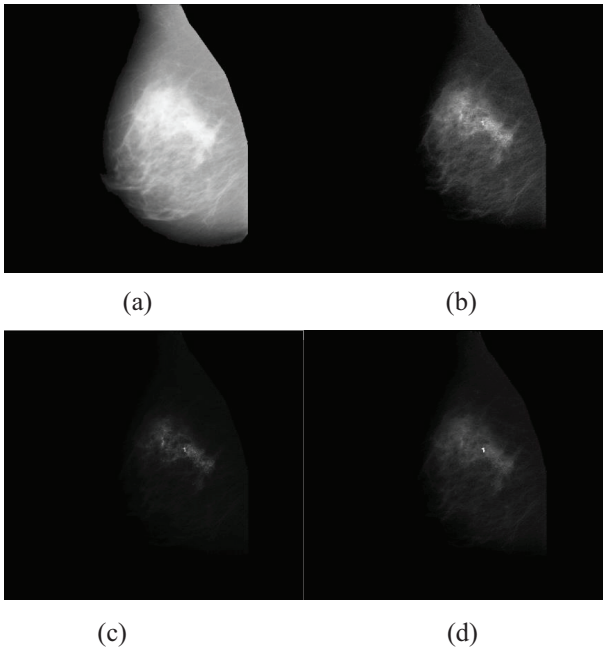

Figure 10. Labeled and positively true classified microcalcification spot in a mammogram image (mdb209): **(a)** original image without pectoral muscles, **(b)** image after ALIE algorithm, **(c)** after the multistable CNN algorithm is applied, **(d)** classified and labeled microcalcification spot in image.

5. Experimental results

To evaluate the proposed algorithm, we used the Mini MIAS database, which is publicly available [22]. The resolution of the images was 200 micron pixels and the size of the images was 1024 × 1024. The database contains 20 images, including 25 microcalcification clusters. The database includes coordinates of the center of the anomaly and the diameter of the surrounding circle. The coordinate system origin is in the bottom left corner.

The final image obtained from the multistable CNN was converted into binary images and the spots were first marked and counted, and then a circle of the anomaly was calculated from these marked spots. The anomaly circles were compared with the circles given in the database. The images were also evaluated and classified by two different radiologists. After this step, we created an ROI set from the images that the radiologists commented on. We selected 100 ROIs for evaluating the classification success. The ROI set consisted of 40 abnormal samples and 60 normal samples. We subjected this dataset to five similar classification methods. These methods were a combination of enhancing techniques and multistable CNN algorithms. Tested classifiers

were ALIE + multistable CNN, CLAHE + multistable CNN, HE + multistable CNN, US + multistable CNN, and multistable CNN without enhancement. Classification performances of the classifiers and the radiologists are presented in Table 2.

Table 2. Performance evaluations of multistable CNN classifiers with image enhancing techniques.

	ALIE + multistable CNN	CLAHE + multistable CNN	HE + multistable CNN	US + multistable CNN	Multistable CNN	Rad. 1	Rad. 2	ALIE + Rad. 1	ALIE + Rad. 2
Number of cases	100	100	100	100	100	100	100	100	100
Number correct	82	36	10	26	47	84	80	89	86
Accuracy	82.0%	36.0%	10.0%	26.0%	47.0%	84.0%	80.0%	89.0%	86.0%
Sensitivity	90.9%	100.0%	0.0%	45.8%	71.0%	85.5%	85.9%	89.0%	88.7%
Specificity	52.2%	13.5%	13.5%	7.7%	7.9%	79.2%	65.5%	88.9%	79.3%
Cases missed	18	64	90	74	53	16	20	11	14
Fitted ROC area	0.853	Degenerate	Degenerate	0.073	0.102	0.93	0.839	0.969	0.92
Empiric ROC area	0.838	0.321	0.055	0.084	0.115	0.918	0.826	0.955	0.905

ROC curves obtained with the proposed method and the other methods using the MIAS database with complete dataset are shown in Figure 11.

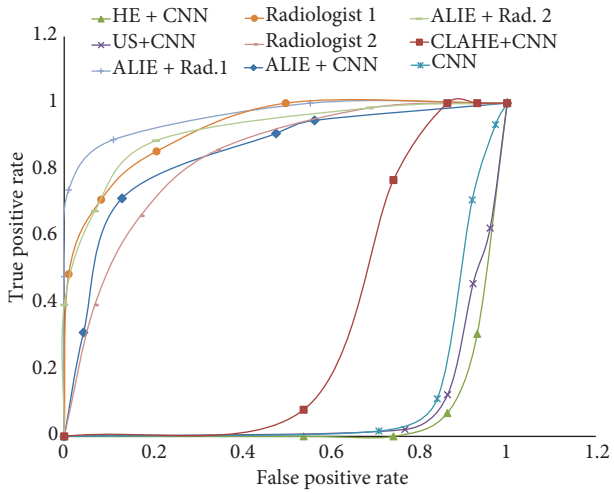

Figure 11. The ROC curves obtained with the proposed method and the other methods using the MIAS database with complete dataset.

As seen in Table 3, the locations detected by the proposed algorithm include or intersect with the original database values. However, we also can see that the algorithm fails on mammogram images of dense breasts.

The character of the background tissue (granularity) is given in Table 3. This information is obtained from the MIAS database [22] as follows:

F: Fatty

G: Fatty-glandular

D: Dense-glandular

Table 3. Locations of anomalies classified by the proposed algorithm.

File name	Granularity	Database default			Raw MIAS (Radiologist 1)			Raw MIAS (Radiologist 2)			MIAS with ALIE (Radiologist 1)			MIAS with ALIE (Radiologist 2)			Proposed algorithm		
		X	Y	Diam.	X	Y	Diam.	X	Y	Diam.	X	Y	Diam.	X	Y	Diam.	X	Y	Diam.
mdb209	G	647	503	87	613	540	146	630	510	200	650	524	128	590	634	126	615	570	9.8
mdb211	G	680	327	13	500	494	94	512	505	108	575	351	73	552	336	85	503	319	60
mdb213	G	547	520	45	540	594	112	532	537	102	565	491	78	544	485	98	554	518	32
mdb216	D	Widely distributed			490 492	486 808	140 220	530	468	132	590	532	252	526	476	108	550	530	664* (wide)
mdb218	G	519	629	8	528	477	136	Not commented			518	448	88	510	450	60	574	400	147
mdb219	G	546	756	29	538	738	184	550	756	72	542	732	144	548	762	76	545	765	10
mdb222	D	398	427	17	Not commented			456	448	156	Not commented			Not commented			535	481	146
mdb223	D	523	482	29	494	480	160	542	478	144	532	490	124	536	54	588	503	499	77
mdb223	D	591	529	6	494	480	160	542	478	144	532	489	124	536	54	588	503	499	77
mdb226	D	287	610	7	520	514	83	Not commented			520	524	78	500	468	90	469	604	138
mdb226	D	329	550	25	340	554	66	Not commented			340	569	60	330	604	77	429	592	116
mdb226	D	531	721	8	330	489	45	Not commented			340	504	30	340	524	43	537	532	267
mdb227	G	504	467	9	534	290	220	522	332	96	518	333	130	522	330	88	521	329	13
mdb231	F	603	538	44	Not commented			Not commented			Not commented			577	495	218	Failed to classify		
mdb233	G	Widely distributed			628	298	264	580	316	288	577	417	140	Not commented			604	284	259* (wide)
mdb236	D	276	824	14	Not commented			Not commented			Not commented			Not commented			Failed to classify		
mdb238	F	522	553	17	510	540	30	512	566	40	525	560	22	523	562	20	447	522	168
mdb239	D	645	755	40	Not commented			Not commented			Not commented			Not commented			Failed to classify		
mdb239	D	567	808	25	Not commented			Not commented			Not commented			Not commented			Failed to classify		
mdb240	D	643	614	23	Not commented			Not commented			Not commented			Not commented			Failed to classify		
mdb241	D	453	678	38	466	672	164	438	404	108	482	662	72	478	692	108	453	610	92
mdb245	F	Widely distributed			622	210	168	612	202	232	620	268	140	620	218	184	643	255	83
mdb248	F	378	601	10	Not commented			Not commented			Not commented			Not commented			378	599	17
mdb249	D	544	508	48	532	638	58	546	625	72	540	623	62	540	613	70	539	507	50
mdb249	D	575	639	64	572	579	30	577	624	45	570	584	32	572	587	38	547	594	112
mdb252	F	439	367	23	Not commented			Not commented			Not commented			Not commented			430	377	56
mdb253	D	733	564	28	725	520	50	742	550	39	730	550	35	730	570	42	714	553	50

In Figure 12, one of the images (mdb241) is evaluated and marked by both radiologists and the proposed algorithm. Figure 12a is the original image labeled with the database's default coordinate values, Figure 12b is the original image labeled by Radiologist 1, Figure 12c is the original image labeled by Radiologist 2, Figure 12d is the enhanced image labeled by Radiologist 1, Figure 12e is the enhanced image labeled by Radiologist 2, and Figure 12f is the original image labeled by the proposed algorithm. Markings of the radiologists were made by hand and the markings of the original database values and our algorithm were made by a computer program.

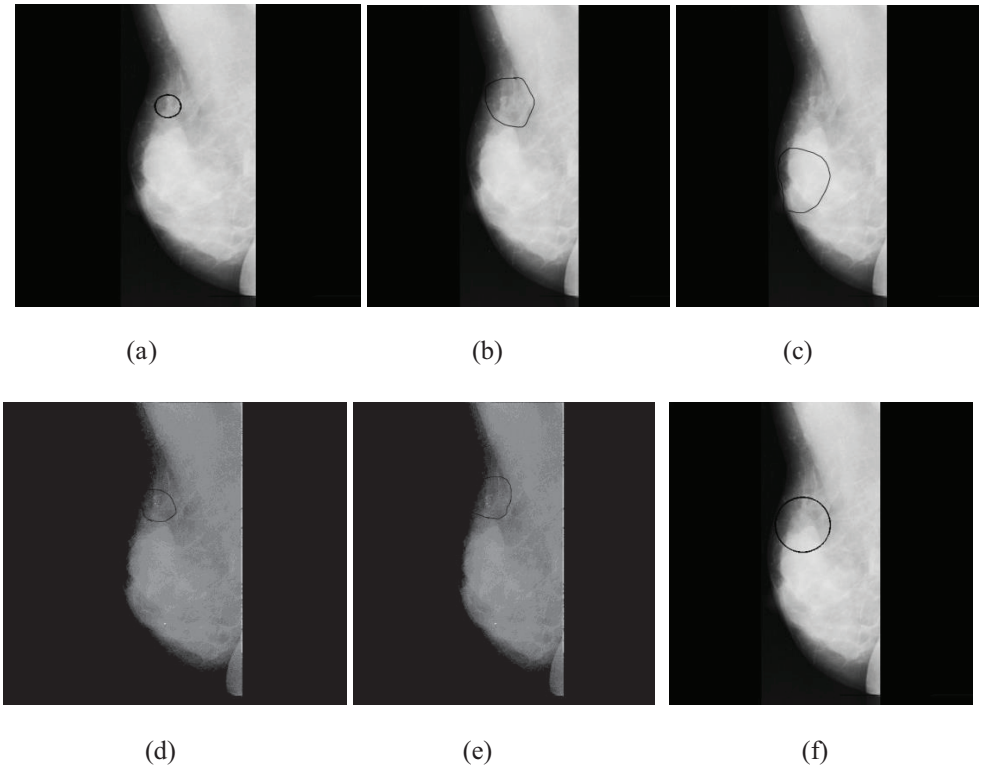

Figure 12. Microcalcification areas labeled by both radiologists and the proposed algorithm in mammogram image (mdb241): **(a)** original image labeled with the database's default coordinate values, **(b)** original image labeled by Radiologist 1, **(c)** original image labeled by Radiologist 2, **(d)** enhanced image labeled by Radiologist 1, **(e)** enhanced image labeled by Radiologist 2, **(f)** original image labeled by the proposed algorithm.

6. Conclusions

In this paper we proposed a new image enhancing method for digital mammograms and a multistable CNN-based classification algorithm for detecting microcalcification spots. The enhancing algorithm prepares the mammogram images for the multistable CNN algorithm. The enhancement algorithm proposed in this paper could be effective in attracting the attention of radiologists to microcalcifications that could be missed at first glance, especially at workload-intensive hospitals. We evaluated our enhancing algorithm with EME, AMBE, and UIQI methods and the algorithm achieved 3.5808 EME score, 38.1757 AMBE score, and 0.5298 UIQI score on average as shown in Table 1. Optimum scores of these evaluation methods mean better enhancing. As seen in Table 1, our method achieved the optimum scores among the other enhancing methods explained in [40–42].

After the enhancement step, our method uses a multistable CNN algorithm for classification of microcalcification spots. There are not enough studies using CNNs in microcalcification detection in mammograms in the literature. The CNN algorithm without enhancement generally fails in microcalcification detection because of the surrounding tissue; our enhancement algorithm significantly reduces this effect and prepares the mammogram image for classification with the CNN algorithm.

To investigate the effect of the enhancement algorithm on classification we compared our method with the following methods: CLAHE + multistable CNN, HE + multistable CNN, US + multistable CNN, and multistable CNN without enhancement. Our method was the most successful among these methods with a 82% accuracy score, as shown in Table 2.

Images were also evaluated and classified by two different radiologists. Radiologist 1 has 12 years of experience in the field and Radiologist 2 has 3 years of experience in the field. The radiologists first evaluated the original MIAS database images (20 images with microcalcifications), and then they evaluated the enhanced images. The evaluation process was done on a normal computer monitor without extra contrast-enhancing capability.

Radiologist 1 achieved 84.0% accuracy in the original MIAS images, and Radiologist 2 achieved 80.0% accuracy in the original MIAS images. After the image enhancement step, Radiologist 1 achieved 89.0% accuracy in enhanced MIAS images, and Radiologist 2 achieved 86.0% accuracy in enhanced MIAS images, as shown in Table 2. Our enhancing algorithm contributed 5% to Radiologist 1 and 6% to Radiologist 2.

However, there are some weaknesses in our technique. The proposed method fails on low density mammogram images and microcalcifications neighboring the pectoral muscle. For increasing the effectiveness of the method, comprehensive clinical studies are in progress.

The proposed algorithm offers new ideas and methods for CNN-based image processing techniques. Integrating this technique with other methods such as genetic algorithms, fuzzy logic, or other classification techniques will bring more precise, robust, and fast results. In the future, we will continue to study our technique and evaluate digital mammogram images. Evaluations will take place on special computer monitors that are used by radiologists for mammogram images.

Acknowledgment

This work is supported by the Coordinatorship of Selçuk University's research projects under Project No. 10101026.

References

[1] Republic of Turkey Ministry of Health Department of Cancer Control. Ulusal Kanser Programı 2009-2015. Ankara, Turkey: Ministry of Health, 2009 (in Turkish).

[2] Darby S, McGale P, Correa C, Taylor C, Arriagada R, Clarke M, Cutter D, Davies C, Ewertz M, Godwin J et al. Effect of radiotherapy after breast-conserving surgery on 10-year recurrence and 15-year breast cancer death: meta-analysis of individual patient data for 10,801 women in 17 randomised trials. Lancet 2011; 378: 1707–1716.

[3] Bouyahia S, Mbainaibeye J, Ellouze N. Computer-aided diagnosis of mammographic images. In: First International Symposium on Control, Communications and Signal Processing; 2004. New York, NY, USA: IEEE. pp. 259–262.

[4] Martin JE, Mokowitz M, Milbrath JR. Breast cancer missed by mammography. AJR Am J Roentgenol 1979; 132: 737–739.

[5] Hernández-Cisneros RR, Yerashima-Marin H. Feature selection for the classification of both individual and clustered microcalcifications in digital mammograms using genetic algorithms. In: A Recombination of the 15th International Conference Genetic Algorithms (ICGA) and the 11th Genetic Programming Conference (GP); Seattle, WA, USA; 2006.

[6] Strauss A, Sebbar S, Desarnaud S, Mouillard Le Gal PM. Automatic detection and segmentation of microcalcifications on digitized mammograms. In: 14^{th} Annual International Conference of the IEEE Engineering in Medicine and Biology Society; 1992. New York, NY, USA: IEEE. pp. 1938–1939.

[7] Jiang J, Yao B, Wason AM. A genetic algorithm design for microcalcification detection and classification in digital mammograms. Comput Med Imag Grap 2007; 31: 49–61.

[8] Wang TC, Karayiannis NB. Detection of microcalcifications in digital mammograms. IEEE T Med Imaging 1998; 17: 498–509.

[9] Sajda P, Spence C, Pearson J. Learning contextual relationships in mammograms using a hierarchical pyramid neural network. IEEE T Med Imaging 2002; 21: 239–250.

[10] Bazzani A, Bevilacqua A, Bollini D, Brancaccio R, Campanini R, Lanconelli N, Riccardi A, Romani D. A SVM classifier to separate false signals from microcalcifications in digital mammograms. Phys Med Biol 2001; 46: 1651–1663.

[11] Szirányi T, Csapodi M. Texture classification and segmentation by cellular neural networks using genetic learning. Comput Vis Image Und 1998; 71: 255–270.

[12] Chua LO, Yang L. Cellular neural networks: theory. IEEE T Circuits Syst 1988; 35: 1257–1272.

[13] Chua LO, Yang L. Cellular neural networks: application. IEEE T Circuits Syst 1988; 35: 1273–1290.

[14] Dogaru R, Murgan AT, Ortmann S, Glesner M. Getting order in chaotic cellular neural networks by self-organization with Hebbian adaptation rules. In: Proceedings of the 1996 Fourth IEEE International Workshop on Cellular Neural Networks and Their Applications; 1996. New York, NY, USA: IEEE. pp. 115–120.

[15] Paasio A, Dawidziuk A, Halonen K, Porra V. About the robustness of CNN linear templates with bipolar images. In: 1996 IEEE International Symposium on Circuits and Systems; 1996. New York, NY, USA: IEEE. pp. 555–557.

[16] Zarandy A, Roska T, Liszka G, Hegyesi J, Kek L, Rekeczky C. Design of analogic CNN algorithms for mammogram analysis. In: Proceedings of the Third IEEE International Workshop on Cellular Neural Networks and Their Applications; 1994. New York, NY, USA: IEEE. pp. 255–260.

[17] Venetianter PL, Roska T. Image compression by cellular neural networks. IEEE T Circuits-I 1998; 45: 205–215.

[18] Zanjun L, Derong L. A new synthesis procedure for a class of cellular neural networks with space-invariant cloning template. IEEE T Circuits-II 1998; 45: 1601–1605.

[19] Matsumoto T, Chua LO, Suzuki H. CNN cloning template: shadow detector. IEEE T Circuits Syst 1990; 37: 1070–1073.

[20] Akbari-Dilmaghani A, Taylor J. Implementation of cellular neural networks with cloning templates of smaller dimensions. In: Proceedings of the Third IEEE International Conference on Electronics, Circuits, and Systems; 1996. New York, NY, USA: IEEE. pp. 410–413.

[21] Giaquinto A, Fornarelli G. PSO-based cloning template design for CNN associative memories. IEEE T Neural Networ 2009; 20: 1837–1841.

[22] Suckling J, Parker J, Dance DR, Astley SM, Hutt I, Boggis CRM, Ricketts I, Stamatakis E, Cerneaz N, Kok SL et al. The mammographic image analysis society digital mammogram database. In: Proceedings of the International Workshop on Digital Mammography; 1994. pp. 211–221.

[23] Kawahara M, Inoue T, Nishio Y. Cellular neural network with dynamic template and its output characteristics. In: Proceedings of International Joint Conference on Neural Networks; Atlanta, GA, USA; 2009. pp. 155–1558.

[24] Perfetti R, Ricci E, Casali D, Costantini G. Cellular neural networks with virtual template expansion for retinal vessel segmentation. IEEE T Circuits Syst 2007; 54: 141–145.

[25] Kozek T, Roska T, Chua LO. Genetic algorithm for CNN template learning. IEEE T Circuits-I 1993; 40: 392–402.

[26] Roska T, Chua LO. CNN: Cellular Analog Programmable Multidimensional Processing Array with Distributed Logic and Memory. Rep. DNS-2-1992. Budapest, Hungary: Computer and Automation Institute of the Hungarian Academy of Sciences, 1992.

[27] Yokosawa K, Nakaguchi T, Tanji Y, Tanaka M. Cellular neural networks with output function having multiple constant regions. IEEE T Circuits-I 2003; 50: 847–857.

[28] Medina Hernandez JA, Castaeda FG, Moreno Cadenas JA. Multistable cellular neural networks and their application to image decomposition. In: 52nd IEEE International Midwest Symposium on Circuits and Systems; 2009. New York, NY, USA: IEEE. pp. 873–876.

[29] Quintanilla-Dominguez J, Cortina-Januchs MG, Ojeda-Magana B, Jevtic A, Vega-Corona A, Andina D. Microcalcification detection applying artificial neural networks and mathematical morphology in digital mammograms. In: Spain World Automation Congress (WAC); 2010. pp. 1–6.

[30] Morrow WM, Paranjape RB, Rangayyan RM, Desautels JEL. Region-based contrast enhancement of mammograms. IEEE T Med Imaging 1992; 11: 392–406.

[31] Chen ZY, Abidi BR, David L, Abidi MA. Gray-level grouping (GLG): an automatic method for optimized image contrast enhancement - Part II: The variations. IEEE T Image Process 2006; 15: 2303–2314.

[32] Panetta KA, Wharton EJ, Agaian SS. Human visual system-based image enhancement and logarithmic contrast measure. IEEE T Syst Man Cy B 2008; 38: 174–188.

[33] Smathers RL, Bush E, Drace J, Stevens M, Sommer FG, Brown BW, Kanas B. Mammographic microcalcifications: detection with xerography, screen-film and digitized film display. Radiology 1986; 159: 673–677.

[34] Kosheleva O, Arenas J, Aguirre M, Mendoza C, Cabrera SD. Compression degradation metrics for analysis of consistency in microcalcification detection. In: IEEE Southwest Symposium on Image Analysis and Interpretation; 1998. New York, NY, USA: IEEE. pp. 35–40.

[35] Thangavel K, Karnan M. Computer aided diagnosis in digital mammograms: detection of microcalcifications by meta-heuristic algorithms. GVIP Journal 2005; 5: 41–55.

[36] Masek M, Chandrasekhar R, deSilva CJS, Attikiouzel Y. Spatially based application of the minimum cross-entropy thresholding algorithm to segment the pectoral muscle in mammograms. In: The Seventh Australian and New Zealand Intelligent Information Systems Conference; 2001. pp. 101–106.

[37] Kwok SM, Chandrasekhar R, Attikiouzel Y, Rickard MT. Automatic pectoral muscle segmentation on mediolateral oblique view mammograms. IEEE T Med Imaging 2004; 23: 1129–1140.

[38] Guzelis C, Karamahmut S. Algorithm for completely stable cellular neural networks. In: Proceedings of the Third IEEE International Workshop on Cellular Neural Network and Applications; Rome, Italy; 1994. pp. 177–182.

[39] Vilariño DL, Cabello D, Pardo XM, Brea VM. Cellular neural networks and active contours: a tool for image segmentation. Image Vision Comput 2003; 21: 189–204.

[40] Grgic S, Grgic M, Mrak M. Reliability of objective picture quality measures. J Electr Eng 2004; 55: 3–10.

[41] Sundaram M, Ramar K, Arumugam N, Prabin G. Histogram modified local contrast enhancement for mammogram images. Appl Soft Comput 2011; 11: 5809–5816.

[42] Wang Z, Bovik AC. A universal image quality index. IEEE Signal Proc Lett 2002; 9: 81–84.

[43] Agaian SS, Lentz KP, Grigoryan AM. A new measure of image enhancement. In: IASTED International Conference on Signal Processing & Communication; 2000.